City Research Online

City, University of London Institutional Repository

Article

Low Magnetic Field Induced Extrinsic Strains in Multifunctional Particulate Composites: An Interrupted Mechanical Strengthening in 3D-Printed Nanocomposites

Andiol Mucolli [1], Alden Midmer [1], Marinos Manolesos [2], Salem Aldosari [3], Cristian Lira [4] and Hamed Yazdani Nezhad [5,*]

1. School of Science and Technology, City, University of London, London EC1V 0HB, UK; andiol.mucolli@city.ac.uk (Andiol Mucolli)
2. School of Mechanical Engineering, National Technical University of Athens, 10682 Athens, Greece; marinos@fluid.mech.ntua.gr
3. Innovation Parks, King Abdulaziz City for Science and Technology, Riyadh 11442, Saudi Arabia; saldosari@kacst.edu.sa
4. Engineering Development, National Composites Centre, Bristol BS16 7FS, UK; cristian.lira@nccuk.com
5. School of Mechanical Engineering, Faculty of Engineering and Physical Sciences, University of Leeds, Leeds LS9 2JT, UK
* Correspondence: h.yazdaninezhad@leeds.ac.uk

Abstract: The current paper reports on the quantification of the effect of magnetic fields on the mechanical performance of ferromagnetic nanocomposites in situ during basic standard tensile testing. The research investigates altering the basic mechanical properties (modulus and strength) via the application of a contact-less magnetic field as a primary attempt for a future composites strengthening mechanism. The nanocomposite specimens were fabricated using filament-based 3D printing and were comprised of ferromagnetic nanoparticle-embedded thermoplastic polymers. The nanoparticles were iron particles dispersed at 21 wt.% (10.2 Vol.%) inside a polylactic acid (PLA) polymer, characterised utilising optical microscopy and 3D X-ray computed tomography. The magnetic field was stationary and produced using permanent neodymium round-shaped magnets available at two field strengths below 1 Tesla. The 3D printing was a MakerBot Replicator machine operating based upon a fused deposition method, which utilised 1.75 mm-diameter filaments made of iron particle-based PLA composites. The magnetic field-equipped tensile tests were accompanied by a real-time digital image correlation technique for localized strain measurements across the specimens at a 10-micron pixel resolution. It was observed that the lateral magnetic field induces a slight Poisson effect on the development of extrinsic strain across the length of the tensile specimens. However, the effect reasonably interferes with the evolution of strain fields via the introduction of localised compressive strains attributed to accumulated magnetic polarisation at the magnetic particles on an extrinsic scale. The theory overestimated the moduli by a factor of approximately 3.1. To enhance the accuracy of its solutions for 3D-printed specimens, it is necessary to incorporate pore considerations into the theoretical derivations. Additionally, a modest 10% increase in ultimate tensile strength was observed during tensile loading. This finding suggests that field-assisted strengthening can be effective for as-received 3D-printed magnetic composites in their solidified state, provided that the material and field are optimally designed and implemented. This approach could propose a viable method for remote field tailoring to strengthen the material by mitigating defects induced during the 3D printing process.

Keywords: magnetic induction; ferromagnetic; multifunctional composite; polymer; 3D printing; magnetic polarisation; mechanical strength

1. Introduction

Magneto-active polymers (e.g., magnetostrictive) are a class of composite materials that consist of a polymer embedded with magnetisable particles, driven by a strain-induced mechanism called magnetic polarisation owing to the dipolar displacement occurring in magnetic and piezomagnetic (magnetostrictive) materials under magnetic field exposure [1–7] serving deformation in soft robotics and actuations [8]. Magnetostriction occurs in almost all ferromagnetic materials such as iron, cobalt, nickel and their corresponding alloys [9]. Particles exhibiting magnetostrictive behaviour are categorised into soft and hard magnetics [10]. A hard magneto-active polymer comprises particles that are magnetised by a magnetic field, with the ability to maintain magnetisation after removing the field, i.e., unloading the material.

Most of the materials are classified as ferromagnetic, paramagnetic and diamagnetic. Ferromagnetic materials have several unpaired electrons on their atoms, generating a relatively weak magnetic field. Individual or groups of atoms randomly align with each other, causing the magnetic field's cancellation, but they are strongly affected by an external magnetic field under which the individual atoms are forced into a specific alignment, which they partially maintain after removing the magnetic field. An external magnetic field slightly attracts paramagnetic materials due to their low number of unpaired electrons on their atoms. Contrary to ferromagnetic materials, they do not sustain magnetic properties after removing the field. Such materials are considered relatively non-magnetic as their magnetic induction is three orders of magnitude lower than that in ferromagnetic materials, generally speaking. Soft ferromagnetic materials are easily magnetised, but their induced magnetism is temporary; they possess low coercive force, high permeability, and thus, minimal hysteresis. Their properties can be enhanced during manufacturing or via heating and annealing. On the other hand, hard ferromagnetic materials require a strong external magnetic field to become magnetized, possessing high coercive force and low permeability. They will maintain their magnetisation unless an opposing magnetic field de-magnetises them.

In soft magneto-active polymers, the particles cannot sustain the magnetisation after the field is removed. Both offer numerous benefits such as multifunctional design, production, and structural flexibility and tailoring [11,12]. Biomedical devices [13,14], field-assisted fabrication [15–17], surgical [18,19], electronics and sensing [20–25], and soft robotics/actuators/stiffening [26–33] are amongst the most common applications for magnetic composite materials. Investigations have been conducted to provide a description of the mechanical properties affected by a magnetic field [34,35]. In soft actuation, elastic magnetic elastomers tested under different field strengths exhibit relatively large viscoelastic deformation [32]. The research suggests a high potential for the exploitation of remote magnetic fields for the introduction of relatively extensive strain (and eventually deformation) in flexible and soft structures. In ciliated surfaces [26,27], high-aspect-ratio miniature pillars are controlled via a magnetic field to alter flow characteristics in fluid-structural interaction applications (e.g., aerodynamic surfaces or internal flow control). It is also noteworthy that magnetic materials deliver a set of additional features used for electromagnetic devices including transformers, sensors and magneto-thermal materials. However, the exploitation of a magnetic field for inducing polarisation mechanisms in polymer composites with relatively higher mechanical strength (and lower elongation) than soft materials, so-called rigid, has not yet been investigated. The current paper investigates the effect of static magnetic fields on the basic mechanical properties of ferromagnetic nanocomposites via quantification of tensile strength and elongation.

Many experiments and investigations have been executed to provide a quantifiable description for mechanical properties under a magnetic field, including (but not limited to) static and standard tests demonstrating uniaxial and biaxial deformation where elastic magnetic elastomers were tested, or large viscoelastic deformation in hard-magnetic soft materials. The interest in natural fibre-reinforced materials, including magneto-active

polymers, is also growing, especially in the automotive industry due to the ongoing legislation in enabling global sustainability.

The current research aims to describe the magnetic-induced strains in rigid magnetic responsive polymer comprising iron particles, at the phenomenological scale, and to quantify the effect of static magnetic fields on the basic mechanical performance. Relatively high strength and stiffness, biodegradable poly-lactic acid (PLA) polymer embedded with micron-level particles has been assessed in the current research. The polymer is utilised abundantly in numerous sectors (e.g., biomedical devices and packaging), and its combination with iron particles extends its ability for applications involving conductive and magnetic lightweight materials.

A commercially available iron particle-embedded PLA filament at fixed particle loading of ~21 wt.% is used for the comparative analysis of the current research (with and without magnetic fields); however, it is noteworthy that the traditional approach of incorporating such fillers is solvent-aided dispersion, where the particles are mixed with solvents to provide better dispersion within a viscous resin, either thermoset or thermoplastic [36–38]. Although, specific to filament productions, extrusion techniques using numerous methods of morphologies (e.g., platelets or else) are available. It is evident that the properties exhibited in a produced filament are significantly affected by the presence of porosity and by the filler distribution [39]. Other approaches to achieve a better dispersion are physical mixing, e.g., ultrasonication, and surface functionalisation of functional fillers such as iron or ceramic. To enhance the compatibility between the inorganic fillers (e.g., iron) and organic polymer (e.g., PLA), researchers use surface hydroxylation via hydrogen peroxide treatment, followed by modification with surface active agents, e.g., silane coupling agents [40]. Such coupling agents add functional groups onto the filler particles' surface that can form covalent bonds with the polymer. It has been widely accepted that functionalities such as electrical conductivity, magnetic permeability and dielectric permittivity increase in nanocomposites with surface-functionalised particles due to the uniform dispersion and lower void content [41]. Pivotal to the current article, iron particles are inexpensive and abundant compared to other magnetic materials, such as rare-earth elements or precious metals. The affordability makes it an attractive candidate for magnetic nanocomposite filaments. The particles can be easily dispersed within thermoplastic matrices such as PLA without impacting the polymer's mechanical properties [42]. The magnetic characteristics of iron particles can be adjusted by modifying factors such as particle size, shape, and concentration within the composite material. This adaptability allows for optimization in the magnetic response of nanocomposite filaments for high-stress application [43].

Quantification of the basic induced properties in magnetically enhanced high-strength polymers may suggest potential for the development of a remote strengthening technology in high-strength materials. To do so, the article has been divided into sections for (1) theoretical derivation of average and localised magnetic field-induced strains in ferromagnetic particulate polymer composite, (2) the particulate composite material and its fabrication via fused deposition modelling (FDM)-based 3D printing [44], (3) magnetic field-equipped basic mechanical testing setup and field evaluation, (4) in-situ strain measurements, and (5) concluding remarks.

2. Theoretical Derivation of Transverse Magnetic Field-Induced Strains in Ferromagnetic Particle-Embedded Polymer Nanocomposite during Longitudinal and Quasi-Static Tensions

A homogenisation method for the theoretical description of a magnetic moment in ferromagnetic particulate polymer nanocomposite has been developed in our former research [16] for the case of high-temperature-softened polymer during 3D printing; however, it will be expanded upon in the current article to incorporate the effects from transversely applied magnetic fields to account for Poisson's ratio in a longitudinally tensioned solid nanocomposite at room temperature.

The proposed formulation assumes that the iron particles are spherical with identical dimensions, distributed uniformly within a polymer matrix at 10.2 Vol.% measured using

X-ray tomography (presented in Section 3). The magnetic and elastic behaviours are fully coupled, which necessitates the derivation of non-linear constitutive equations. However, to simplify the complexity associated with such non-linearity, an innovative approach is introduced to decouple the mechanical and magnetic constitutive equations. Given the inherent coupling of the magnetostrictive material, we introduce this behaviour into our model through the stress induced by the magnetic field on the composite. This is achieved by considering the Lorentz force acting on each individual iron particle. Furthermore, the Mori–Tanaka model, one of the mean-field homogenisation techniques, is utilised to investigate the effective compliance matrix of the particulate composite. Therefore, strain induced in the magnetic composite subjected to a unidirectional magnetic field is obtained by:

$$
\begin{Bmatrix}
\varepsilon_x \\
\varepsilon_y \\
\varepsilon_z \\
2\varepsilon_{xy} \\
2\varepsilon_{yz} \\
2\varepsilon_{xz}
\end{Bmatrix}
= [S_{eq}]
\begin{Bmatrix}
0 \\
0 \\
\sigma_z \\
0 \\
0 \\
0
\end{Bmatrix},
\tag{1}
$$

where σ_z is the sole stress induced by the magnetic field in the transverse (z) direction, and S_{eq} is the compliance matrix described in [16].

In the current article, quasi-static tensile tests have been conducted on the nanocomposite specimens, where mechanical load is applied longitudinally on dogbone standard test specimens, generating σ_T stress, while static magnetic fields are applied transversely (i.e., perpendicular to the longitudinal direction) to examine the interruption caused by the field on the mechanical response. Equation (1) is then modified as follows to incorporate the effect of a transversely induced field on the longitudinal properties via Poisson's behaviour:

$$
\begin{Bmatrix}
\varepsilon_x \\
\varepsilon_y \\
\varepsilon_z \\
2\varepsilon_{xy} \\
2\varepsilon_{yz} \\
2\varepsilon_{xz}
\end{Bmatrix}
= [S_{eq}]
\begin{Bmatrix}
\sigma_T \\
0 \\
\sigma_z - v_{eff}\ \sigma_T \\
0 \\
0 \\
0
\end{Bmatrix}
\tag{2}
$$

In Equation (2), v_{eff} denotes the effective Poisson's ratio of the particulate composite. For the composites examined with a relatively low volume fraction of particles, v_{eff} is approximated to the Poisson's ratio of the polymer material. Accordingly, a code has been developed and populated for the calculations (see a link to access the code under Acknowledgments).

3. Materials and Experiments

In this study, 21 wt.% iron particulate PLA filaments (diameter: 1.75 mm) supplied by Amolen were used for 3D printing tensile test dogbone specimens designed according to Standard ASTM D638 [45]. This particular filament was selected based upon two selection criteria: (i) good quality particulate polymer filament within an acceptable dimensional tolerance reliable for continuous FDM 3D-printing without the introduction of disruptions such as discontinuity during the printing, and (ii) well-dispersed micron-level particles (our observation showed that more than 70% of particles distributed in this filament are within 5–10 microns). The 21 wt.% filament type was selected as a fixed case study for our comparative analysis (with and without magnetic fields).

An FDM MakerBot Replicator 2X printer was utilised to fabricate the specimens according to the dimensions in Figure 1a. The temperatures during the 3D printing (extruder and bed temperatures) were carefully tuned to minimise the disbonding between layers and process-induced curvature in the specimens. This was achieved initially via adopting the recommended temperatures by the supplier and then via trial and error followed by optical

microscopy observation of the specimens fabricated in several iterations. Our observations via optical microscopy also showed the broad range of dispersion and distribution density of iron particles in the specimen (Figure 1b,c). The agglomerated particles in mesoscale as such may reduce the mechanical strength at phenomenological levels. We did not have control of such agglomeration since the material was commercially supplied by Amolen; however, quantifications of the particles' size were conducted. To quantify the level of the particle density, 3D X-ray computed tomography (XCT) was also conducted (results presented and discussed later in the current section).
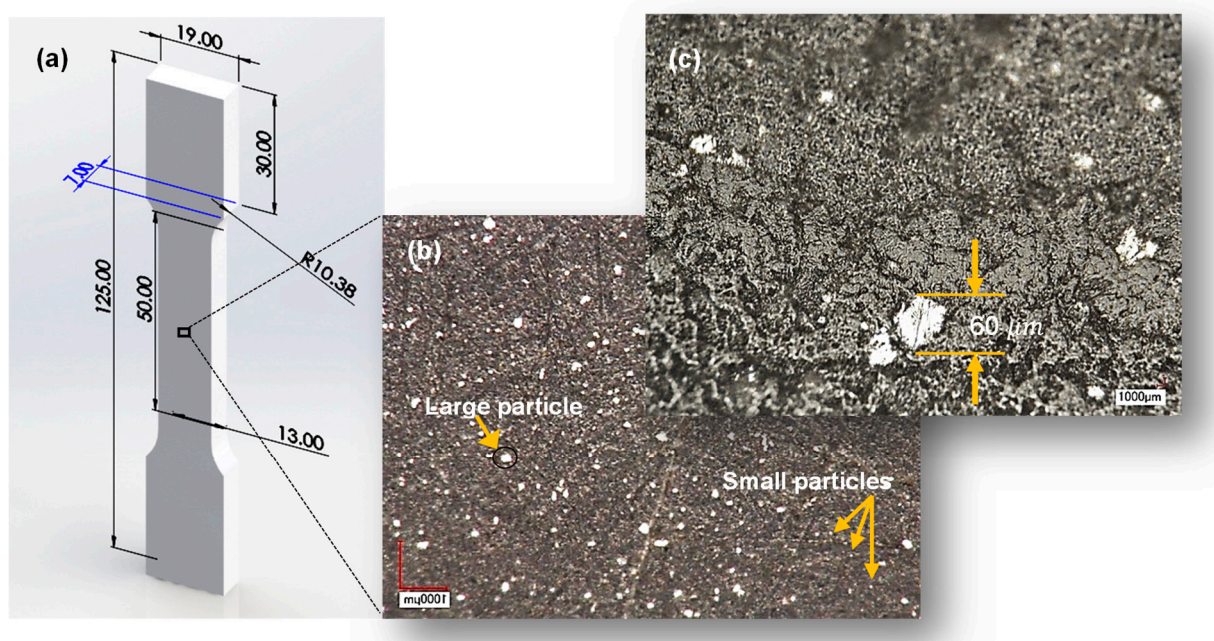
Figure 1. (**a**) ASTM D638 specimen (dimensions in mm), (**b**,**c**) optical microscopic images of 3D-printed tensile iron particle PLA-based nanocomposites.

The final parameter settings for repeatable 3D-printing of the 1.7 mm-diameter filaments using a ~0.4 mm 3D-printing nozzle diameter were:

- Extruder temperature: 220 °C,
- Bed temperature: 60 °C,
- Travel Speed: 50 mm/min,
- Z-axis travel speed: 23 mm/min,
- Layer height: 0.20 mm.

Figure 2a presents images for the steps of the 3D printing. Faulty-produced specimens (distorted and disbonded layers) are shown in Figure 2b prior to the stage where the final setting parameters were used. Optimal quality produced specimens after implementing the final settings (control parameters identified above) are presented in Figure 2c, which were trimmed to meet the standard dimensions required for tensile testing.

Microscopic images from the 3D-printed specimens showed a nearly uniform distribution of the iron particles inside the PLA (using a VHX Digital Microscope). The particle size was broadly varied between approximately 10 and 100 microns (Figure 1b,c). The microstructural analysis performed using 3D X-ray Computed Tomography (XCT), presented in Figure 3, showed that most particles ($\approx$70%) have a 10 micron diameter and a particle distribution quality of 10.2 Vol.%. Particles with size < 10 micron are rarely present in the filament and the printed specimens and thus have been neglected. Further analysis using I13 Diamond light-source's 3D XCT at a 0.8 micron resolution, post-processed by ImageJ software ver. 1.54i, showed that the distribution quality observed via microscopy is maintained (approximately) through the thickness of the printed specimen.

Figure 2. (**a**) Typical 3D printing strategy used, (**b**) faulty-produced specimens with distortion and disbonding, (**c**) optimally produced specimens using the final 3D printing parameter settings.

Nine optimal specimens were produced and tested using an Instron tensile test machine with and without stationary magnetic field application. The tests were conducted under the speed rate of 40 mm/min. Two types of Neodymium magnets were used: 1–10 mm-diameter round magnets possessing magnetic intensity of approx. 0.15 T (shown in Figure 4), and 2–4 mm-diameter ones possessing an intensity of approx. 0.17 T, as measured by an SDL 900 Magnetic Meter supplied by Extech Instruments. An approximately ~300 mT maximum application was reached with 3-row 150 mT magnets in columnar placements to cover the 50 mm specimen's gauge length, as seen in the figure (note that the increase in the field is not proportional to the increase in the number of magnets used). Thin metallic sheets were used to fix the composite magnets on two sides. The tests were also accompanied by a digital image correlation (DIC) facility for real-time surface strain measurements (at a speed of 500 frames per second). One side of the specimens was speckled for the DIC measurements.
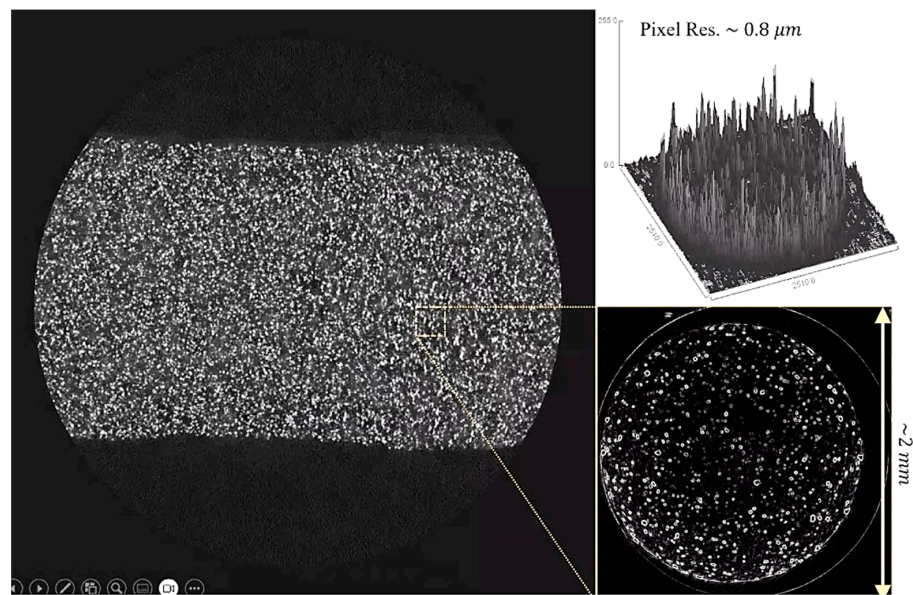
Figure 3. Typical 3D XCT observation of the 21 wt.% iron particle-embedded PLA examined in the current research.
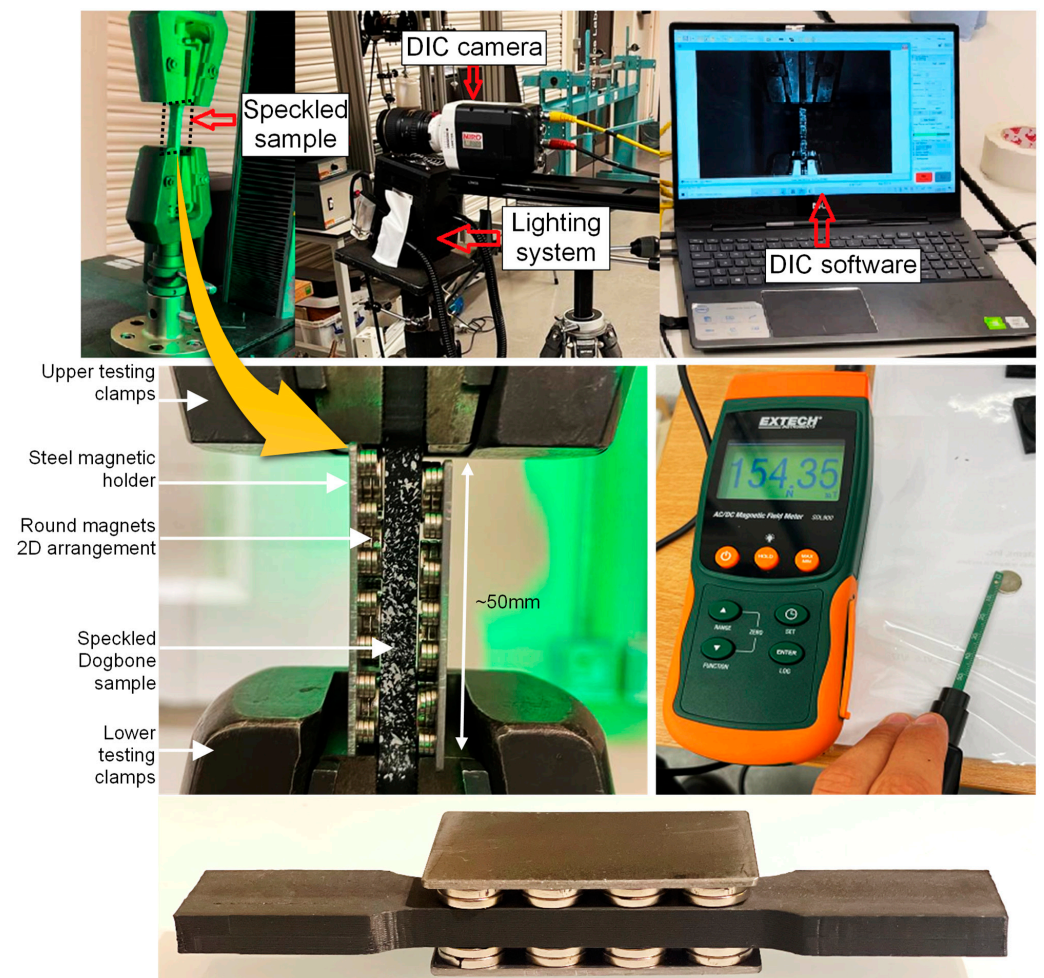

Figure 4. Magnetic field-equipped tensile test setup in situ with DIC measurement.

4. Results and Discussion

4.1. Phenomenological Mechanical Response of Magnetic Field-Assisted Nanocomposite Specimens

Figure 5 shows the engineering strain–stress data for the specimens tested representing three different test categories:

- Category 1 tests where no external magnetic field was applied,
- Category 2 tests in the presence of a 'weak' magnetic field (~170 mT),
- Category 3 tests where the 'strong' field was used (~300 mT).
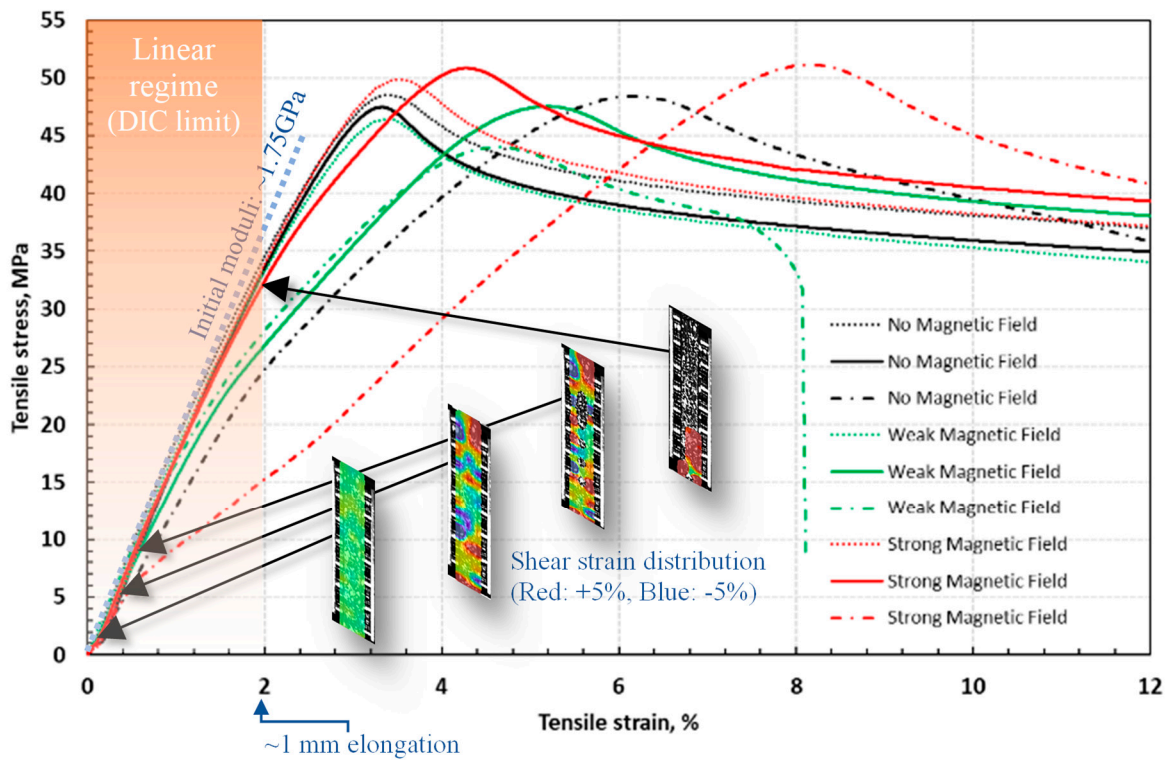
Figure 5. Strain–stress data from tensile testing of the nanocomposite samples under zero, weak and strong magnetic fields.

Data from categories 1, 2 and 3 are shown with black, green and red curves, respectively.

The initial (elastic) moduli exhibited by all specimens did not show any noticeable difference with or without an external magnetic field (approx. 1.75 GPa). All specimens followed a linear and approximately similar trend with this moduli up to ~2% strains after which nonlinearity is observed at ~32 MPa for the majority of the specimens, at which the initial moduli is slightly (~28%) reduced, except for the specimen shown by a dot-dashed red line exhibiting initial nonlinearity at 0.45% (attributed to the different microstructure induced by fabrication uncertainty). Our observations showed relatively higher volumes of polymer-rich area; however, the reason behind such Vol.% disparity was not identified. Moreover, there are disparities observed in the curves. The control parameters during the fabrication were constant for all specimens except for the time at which specimens were printed, and this specific specimen was the last one produced. The filament's multi-material distribution quality may also contribute to such disparity when printing of the material at relatively lower thermal conductivity is performed, thus affecting the quality of the specimens.

All specimens experienced yield stresses at strains > 3.2% at which the slope is reduced to zero. The specimens exhibiting disparity for the nonlinearity regime prior to yielding the strain at which they yield significantly differ from one another; however, the stress falls within the same range as that for others.

The majority of the specimens under no magnetic field (dark curves) and under weak field (green) exhibit approximately similar levels of yield stress, i.e., 44–48 MPa, at strains above 3.3% (four at 3.3%, 2 at 4.8% and 1 at 6.2%). On the other hand, the specimens under the strong field (red curves) exhibit higher yield stress and strain, i.e., >51 MPa and >3.6%, respectively, with one distinctive specimen yielding 52 MPa and 8.2% strain. Though insignificant, the strong field application in situ during the tensile testing has led to higher yield and ultimate stresses. The theoretical descriptions provided in Section 2 are for the linear elastic regime and do not provide descriptions for the effects on the yield and ultimate stresses; however, this is attributed to the field becoming more effective than the weak field for the introduction of field-induced strain energy (dominantly near the surface of the samples) and stress–strain tensors in an opposing direction to the longitudinal tensile loads. Though further investigation is required, the mechanism shall act as a compressive pre-stressing method to hinder the coalescence and creation of pores and cracks embarking at the yield point and progressing toward the ultimate stress point.

We cannot reach a definite statement over the observations from no field tests and weak field tests. However, the specimens under the 300 mT ('strong') field clearly exhibit an ~18% increase in yield stress compared to that in specimens without a field application. All specimens exhibited very high elongation at ultimate failure. Figure 6 shows the side view of one typical specimen after its failure and a number of typical ultimate failure points. A dramatic distortion is observed on the speckles and the specimen that invalidated the DIC data at such high strains beyond the peak strains (>8%). Therefore, a description of the effect of the field on the failure mechanism could not be provided solely based on the DIC data.
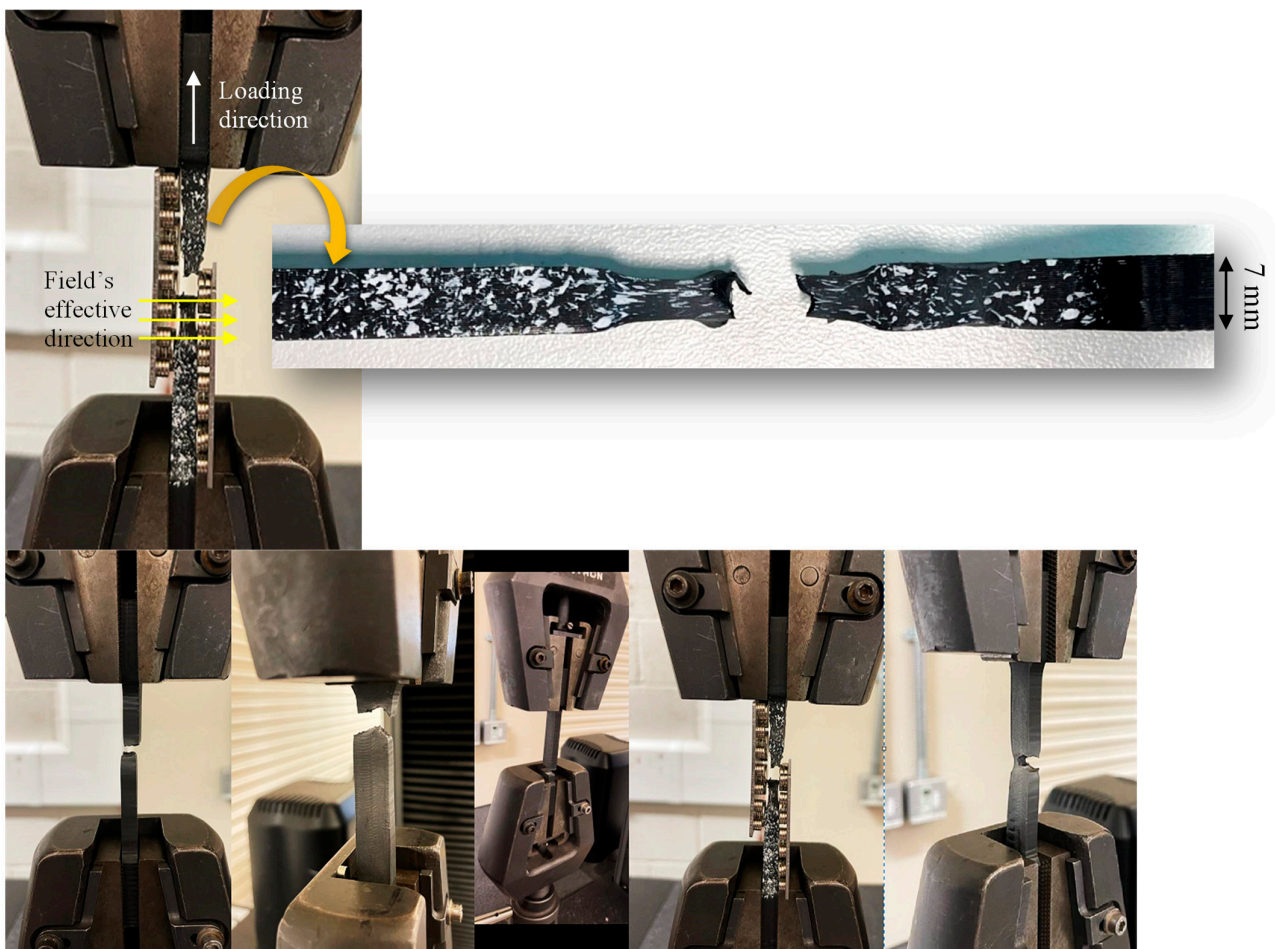
Figure 6. Typical specimen with speckled surface (for DIC measurements) at its ultimate failure point.

It is noteworthy that the factor of the field's depth of penetration plays a significant role in the level of polarisation-induced strains on the relatively thick specimens examined here, as also observed as a major player in electromagnetic field-induced strains [6,46,47]. To realise this further, Figure 7 presents the 262 mT magnetic field-induced pattern developing within the magnetic composite specimens before tensile testing. It is seen that the magnetic field decays significantly when penetrating through the specimens to ~47 mT (nearly 82% reduction). Such measurements show that nearly 80% reduction in the field strength occurs at ~2 mm depth from the specimen surface, i.e., ~20% is only received at the specimen's central axis at a depth of ~3.5 mm. This implies an apparent indication that iron particles possessing significantly higher magnetic properties than the polymer, develop a significant near-surface magnetic moment, which dissipates the field energy to strain energy.


Figure 7. Magnetic field's pattern of 2-row neodymium magnets and depth of penetration in the magnetic composite specimen; measurements showing nearly 82% reduction in the field strength over ~2 mm depth from the specimen surface, i.e., ~20% is induced at the specimen centre.

Such phenomena may be interconnected with the poor depth of penetration, which contributes to the insignificant increase in the yield stresses under the strong field during the tensile testing (Figure 5). The other factor contributing to the reduction in the effectiveness of the field is the direction of the field with respect to the direction currently perpendicular to the loading direction. Poison's ratio (~0.3) is the major driver (and multiplier in the stress–strain governing equation) accounting for the through-thickness polarisation-induced strain in the strains developing in the loading direction. It is anticipated that the field application in a direction parallel to the loading direction would have had a significant effect on the yield stress above 18%.

4.2. In-Situ DIC Measurements of Magnetic Field Equipped Tensile Testing

The in-situ DIC measurement was conducted on specimens with and without magnetic fields; however, the strong field was only used for such measurements since the tests with the weak field exhibited a slight change in the yield stress. As mentioned in the previous section, the specimens were elongated significantly beyond the yield point, which largely stretched their speckled surfaces (Figure 6) and therefore invalidated the DIC data post-yielding points. Therefore, the strain gradients measured by the DIC have been presented only for the linear stage of the strain–stress curves, also shown in Figure 5. The following figures present a comparative analysis of the strain data evolving under ~300 mT in the 5 mm-thickness specimens.

The evolution of shear strains across the specimen, with and without the magnetic field application, is shown in Figures 8–10. As mentioned before, the DIC could only observe the initial loading conditions within the linear regime, e.g., the strain gradient was not obtained at or after a 1.5 mm displacement. The strains were varied from 0.05 mm to 0.23 mm, for both specimens with and without the magnetic fields. The specimen with no magnetic field shows a relatively uniform distribution of strains across the length and width of it (note that the noise from the background environment captured by the DIC as a coloured pattern beyond the specimen's boundaries has been ignored in our investigations). The specimen under the magnetic fields, on the other hand, exhibits non-uniform distribution of strains evolving with the increasing applied displacement. An exchange of positive and negative strain values at regions local to the round magnets is apparent, indicating the presence of magnetic field-induced polarisation. Such effect would not be assumed to be fortuitous, given the comparative analysis with the tests without magnetic fields and the repetitive observations in other specimens; however, the effect of the polarisation on the development of alternating strains in the areas local to stationary magnets is surprising and would require further investigations. In former research by the authors, the compressive strain was developed in dielectric polymer nanocomposites when subjected to electromagnetic induction, owing to the dielectric polarisation developed by the domain walls movement [6]. It is envisaged that such phenomena might be playing a role in the introduction of the compressive strain regions; however, it would require further microstructural investigations.
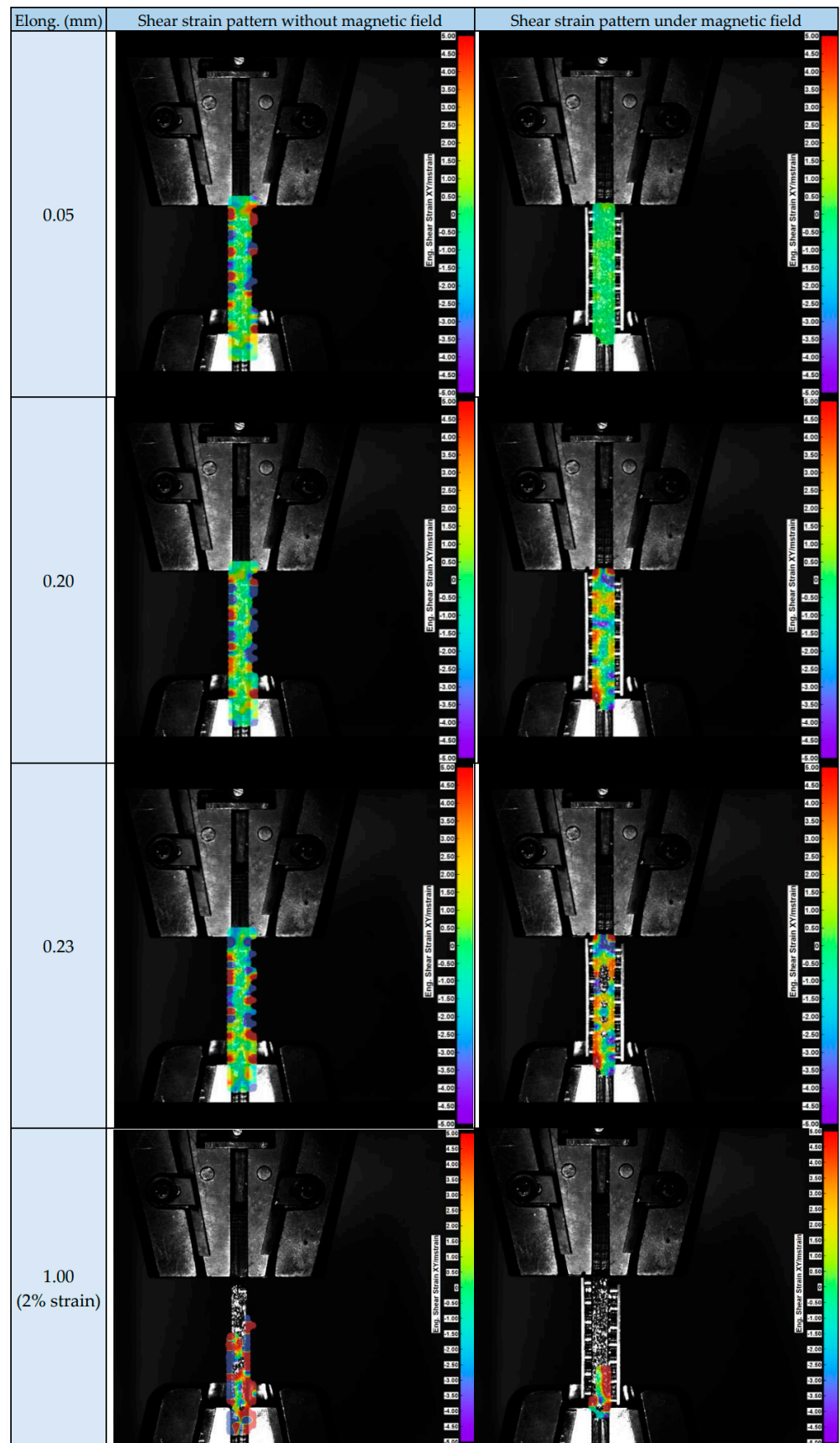
Figure 8. Evolution of shear strains in the specimens with and without magnetic fields during the DIC-equipped tensile tests.
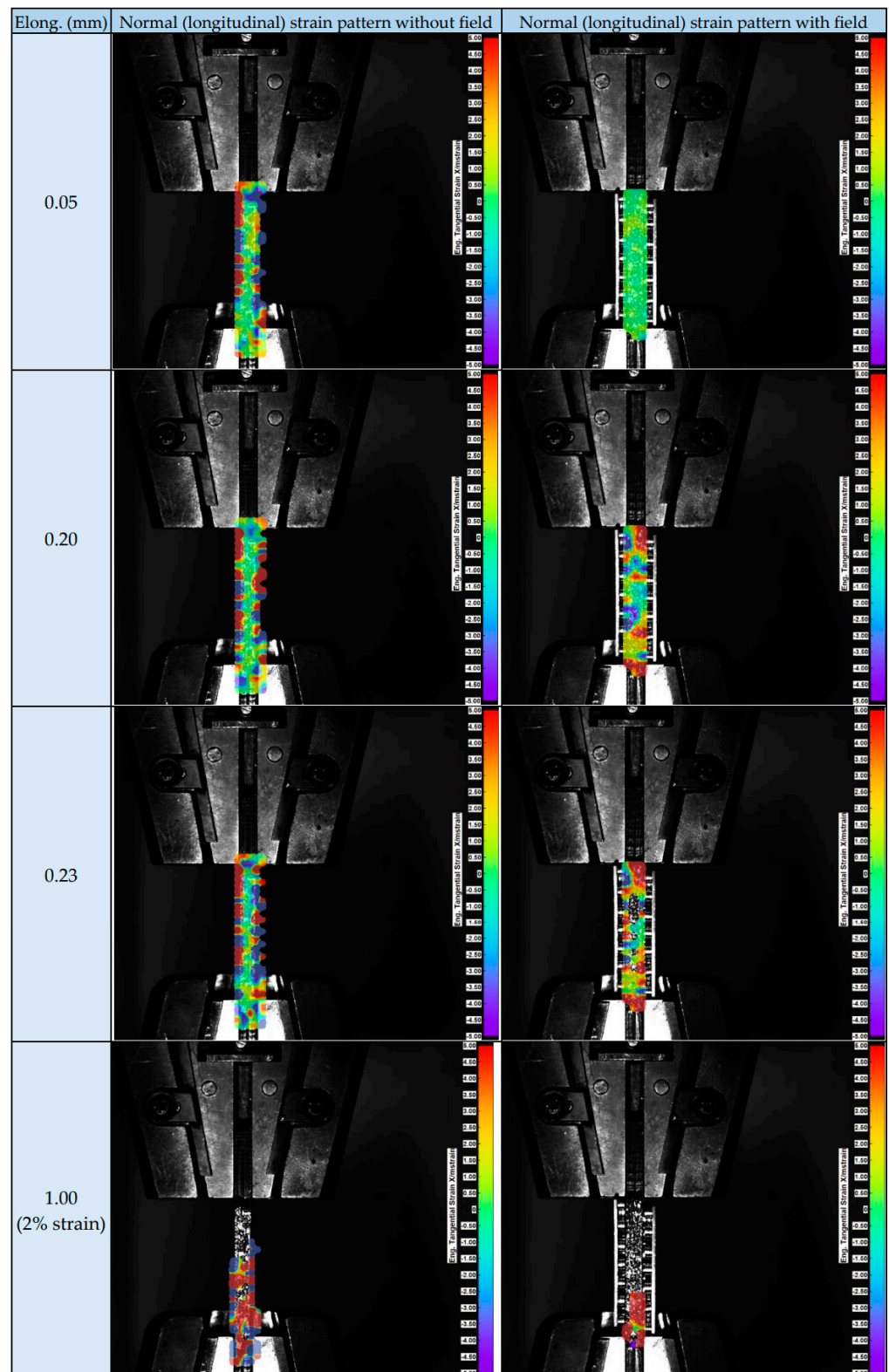
Figure 9. Evolution of normal strains (towards the longitudinal direction) in the specimens with and without magnetic field application during the DIC-equipped tensile tests.
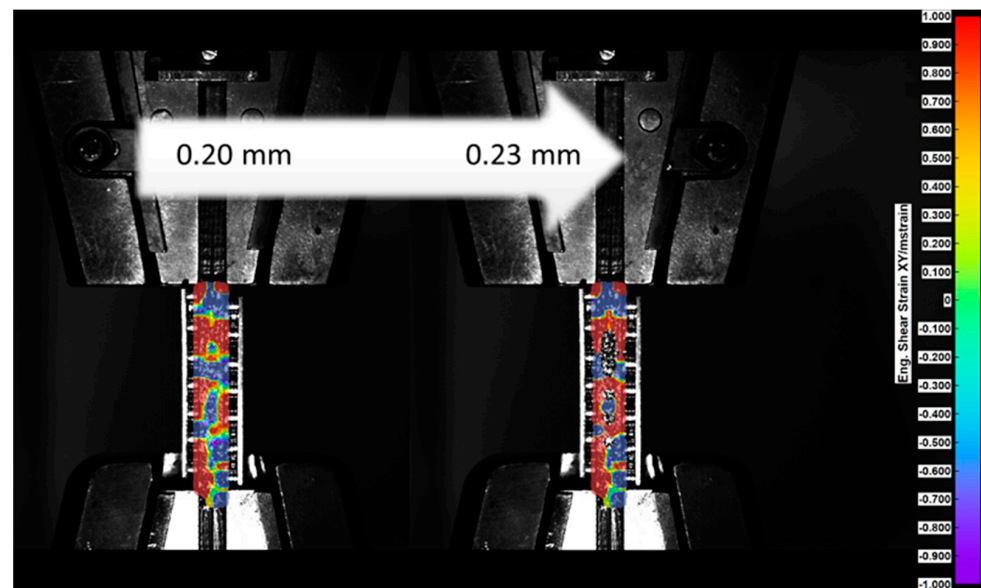
Figure 10. Shear strains developing under magnetic field application at 0.20 mm and 0.23 mm applied displacements, within ±1.00 microstrain range (±0.1%)), presenting evolving compressive strains during the tensile testing (i.e., alternating maximum strain areas—blue and red areas, dominating green areas).

5. Conclusions

The research reported on the trivial effect of a relatively low magnetic field (<1 T) transversely interrupted the longitudinally loaded, 3D-printed, rigid magnetic composites (iron particles embedded PLA) at room temperature, applied in situ during a standard quasi-static tensile loading and perpendicularly to the loading direction. Such effect has formerly been reported to be significant in such composite under high-temperature processes, such as 3D printing, where the PLA is inclined to soften. The tests were conducted under low field strengths of <1-Tesla. A theoretical formulation was derived to describe the linear elastic response in an ideally solid composite. DIC was conducted for extrinsic strain evaluations across the specimens. It was observed that despite the trivial increase in the yield and ultimate stresses (~10%), the low magnetic field induces non-linear strain variations across the width and length of the specimens, which could interfere with the evolution of the strain fields occurring at phenomenological scale, across the length. However, such field-induced extrinsic strains observed via DIC in action during the tensile loading had a minimal effect on the tensile moduli (through manipulating longitudinal strains with the Poisson ratio effects), which was also validated by the theory. The theory also overestimated the moduli by the order of 3.1 times. This would necessitate an incorporation of pores in the theoretical derivations to improve the accuracy of its solution for the 3D-printed specimens. Moreover, a trivial 10% increase at the ultimate tensile strength was observed during the tensile loading. This would suggest that the field-assisted strengthening can be effective for as-received 3D-printed magnetic composites post-processing in their solidified state if only the material and field are optimally designed and implemented to propose viable remote field tailoring for strengthening via suppressing 3D-printing-induced defects.

Conflicts of Interest: The authors declare no conflict of interest.

References

1. Rajan, A.; Arockiarajan, A. Bending of hard-magnetic soft beams: A finite elasticity approach with anticlastic bending. *Eur. J. Mech.-A/Solids* **2021**, *90*, 104374. [CrossRef]
2. Singh, R.P.; Onck, P.R. Magnetic field induced deformation and buckling of slender bodies. *Int. J. Solids Struct.* **2018**, *143*, 29–58. [CrossRef]
3. Kalita, V.M.; Dzhezherya, Y.I.; Cherepov, S.V.; Skirta, Y.B.; Bodnaruk, A.V.; Ryabchenko, S.M. Spontaneous change of symmetry in a magnetoactive elastomer beam at its critical bending induced by a magnetic field. *Smart Mater. Struct.* **2023**, *32*, 045002. [CrossRef]
4. Moreno-Mateos, M.A.; Danas, K.; Garcia-Gonzalez, D. Influence of magnetic boundary conditions on the quantitative modelling of magnetorheological elastomers. *Mech. Mater.* **2023**, *184*, 104742. [CrossRef]
5. Kalina, K.A.; Gebhart, P.; Brummund, J.; Linden, L.; Sun, W.C.; Kästner, M. Neural network-based multiscale modeling of finite strain magneto-elasticity with relaxed convexity criteria. *Comput. Methods Appl. Mech. Eng.* **2024**, *421*, 116739. [CrossRef]
6. Li, D.; Barrington, J.; James, S.; Ayre, D.; Słoma, M.; Lin, M.F.; Yazdani Nezhad, H. Electromagnetic field controlled domain wall displacement for induced strain tailoring in $BaTiO_3$-epoxy nanocomposite. *Sci. Rep.* **2022**, *12*, 7504. [CrossRef]
7. Pearson, C.; Hawi, S.; Lira, C.; Goel, S.; Yazdani Nezhad, H. Magnetic field assisted 3D printing of short carbon fibre-reinforced polymer composites. *Mater. Today Proc.* **2022**, *64*, 3. [CrossRef]
8. Sratong-on, P.; Chernenko, V.A.; Feuchtwanger, J.; Hosoda, H. Magnetic field-induced rubber-like behavior in Ni-Mn-Ga particles/polymer composite. *Sci. Rep.* **2019**, *9*, 3443. [CrossRef]
9. *Std 319-1971*; IEEE Standard on Magnetostrictive Materials. Technical Committee on Transducers and Resonators. The Institute of Electrical and Electronics Engineers, Inc.: Piscataway, NJ, USA, 1971.
10. Kadapa, C.; Hossain, M. A unified numerical approach for soft to hard magneto-viscoelasticity coupled polymers. *Mech. Mater.* **2022**, *166*, 104207. [CrossRef]
11. Zhang, C.; Li, X.; Jiang, L.; Tang, D.; Xu, H.; Zhao, P.; Fu, J.; Zhou, Q.; Chen, Y. 3D Printing of Functional Magnetic Materials: From Design to Applications. *Adv. Funct. Mater.* **2021**, *31*, 2102777. [CrossRef]
12. Stepanov, G.V.; Abramchuk, S.S.; Grishin, D.A.; Nikitin, L.V.; Kamarenko, E.Y.; Khokhlov, A.R. Effect of a homogeneous magnetic field on the viscoelastic behavior of magnetic elastomers. *Polymer* **2007**, *48*, 488–495. [CrossRef]
13. Plen, R.; Smith, A.; Blum, O.; Aloni, O.; Locker, U.; Shapira, Z.; Margel, S.; Shefi, O. Bioengineering 3D Neural Networks Using Magnetic Manipulations. *Adv. Funct. Mater.* **2022**, *32*, 2204925. [CrossRef]
14. Chen, J.C.; Bhave, G.; Alrashdan, F.; Dhuliyawalla, A.; Hogan, K.J.; Mikos, A.G.; Robinson, J.T. Self-rectifying magnetoelectric metamaterials for remote neural stimulation and motor function restoration. *Nat. Mater.* **2024**, *23*, 139–146. [CrossRef]
15. Zhou, X.; Ren, L.; Liu, Q.; Song, Z.; Wu, Q.; He, Y.; Li, B.; Ren, L. Advances in Field-Assisted 3D Printing of Bio-Inspired Composites: From Bioprototyping to Manufacturing. *Macromol. Biosci.* **2022**, *22*, 2100332. [CrossRef]
16. Afshari, P.; Pavlyuk, M.; Lira, C.; Katnam, K.-B.; Bodaghi, M.; Nezhad, H.Y. Mechanical Strain Tailoring via Magnetic Field Assisted 3D Printing of Iron Particles Embedded Polymer Nanocomposites. *Macromol. Mater. Eng.* **2023**, *308*, 2300194. [CrossRef]
17. Pishvar, M.; Amirkhosravi, M.; Altan, M.C. Magnet Assisted Composite Manufacturing: A Flexible New Technique for Achieving High Consolidation Pressure in Vacuum Bag/Lay-Up Processes. *J. Vis. Exp.* **2018**, *135*, 57254. [CrossRef] [PubMed]
18. Lloyd, P.; Dall'Armellina, E.; Schneider, J.E.; Valdastri, P. Future cardiovascular healthcare via magnetic resonance imaging-driven robotics. *Eur. Heart J.* **2024**, ehae095. [CrossRef]
19. Koszowska, Z.; Brockdorff, M.; da Veiga, T.; Pittiglio, G.; Lloyd, P.; Khan-White, T.; Harris, R.A.; Moor, J.W.; Chandler, J.H.; Valdastri, P. Independently Actuated Soft Magnetic Manipulators for Bimanual Operations in Confined Anatomical Cavities. *Adv. Intell. Syst.* **2024**, *6*, 2470009. [CrossRef]

20. Ciorciaro, L.; Smoleński, T.; Morera, I.; Kiper, N.; Hiestand, S.; Kroner, M.; Zhang, Y.; Watanabe, K.; Taniguchi, T.; Demler, E.; et al. Kinetic magnetism in triangular moiré materials. *Nature* **2023**, *623*, 509–513. [CrossRef]

21. Boix-Constant, C.; Jenkins, S.; Rama-Eiroa, R.; Santos, E.J.; Mañas-Valero, S.; Coronado, E. Multistep magnetization switching in orthogonally twisted ferromagnetic monolayers. *Nat. Mater.* **2023**, *23*, 212–218. [CrossRef]

22. Tang, C.; Alahmed, L.; Mahdi, M.; Xiong, Y.; Inman, J.; McLaughlin, N.J.; Zollitsch, C.; Kim, T.H.; Du, C.R.; Kurebayashi, H.; et al. Spin dynamics in van der Waals magnetic systems. *Phys. Rep.* **2023**, *1032*, 1–36. [CrossRef]

23. Babicheva, V.E.; Moloney, J.V. Lattice effect influence on the electric and magnetic dipole resonance overlap in a disk array. *Nanophotonics* **2018**, *7*, 1663–1668. [CrossRef]

24. Mudhar, R.; Mucolli, A.; Ford, J.; Lira, C.; Yazdani Nezhad, H. Electrical and Magnetic Properties of 3D Printed Integrated Conductive Biodegradable Polymer Nanocomposites for Sustainable Electronics Development. *J. Compos. Sci.* **2022**, *6*, 345. [CrossRef]

25. Huxter, W.S.; Palm, M.L.; Davis, M.L.; Welter, P.; Lambert, C.-H.; Trassin, M.; Degen, C.L. Scanning gradiometry with a single spin quantum magnetometer. *Nat. Commun.* **2022**, *13*, 376. [CrossRef]

26. Cui, Z.; Wang, Y.; Zhang, S.; Wang, T.; den Toonder, J.M.J. Miniaturized metachronal magnetic artificial cilia. *Proc. Natl. Acad. Sci. USA* **2023**, *120*, e2304519120. [CrossRef]

27. Han, J.; Dong, X.; Yin, Z.; Zhang, S.; Li, M.; Zheng, Z.; Ugurlu, M.C.; Jiang, W.; Liu, H.; Sitti, M. Actuation-enhanced multifunctional sensing and information recognition by magnetic artificial cilia arrays. *Proc. Natl. Acad. Sci. USA* **2023**, *120*, e2308301120. [CrossRef]

28. Bastola, A.K.; Gannavarapu, M.; Parry, L.A.; Shrestha, M. Magnetorheological brushes–Scarcely explored class of magnetic material. *J. Magn. Magn. Mater.* **2023**, *572*, 170603. [CrossRef]

29. Sakuma, H. Three-dimensional motion control of an untethered magnetic object using three rotating permanent magnets. *Sci. Rep.* **2023**, *13*, 18052. [CrossRef]

30. Barron, E.J.; Williams, E.T.; Tutika, R.; Lazarus, N.; Bartlett, M. A unified understanding of magnetorheological elastomers for rapid and extreme stiffness tuning. *RSC Appl. Polym.* **2023**, *1*, 315–324. [CrossRef]

31. Bastola, A.; Hossain, M. The shape-morphing performance of magnetoactive soft materials. *Mater. Des.* **2021**, *211*, 110172. [CrossRef]

32. Dadgar-Rad, F.; Mokarram, H. Large viscoelastic deformation of hard-magnetic soft beams. *Extrem. Mech. Lett.* **2022**, *54*, 101773. [CrossRef]

33. Moreno-Mateos, M.A.; Hossain, M.; Steinmann, P.; Garcia-Gonzalez, D. Hybrid magnetorheological elastomers enable versatile soft actuators. *Npj Comput. Mater.* **2022**, *8*, 162. [CrossRef]

34. Garcia-Gonzalez, D.; Ter-Yesayants, T.; Moreno-Mateos, M.A.; Lopez-Donaire, M.L. Hard-magnetic phenomena enable autonomous self-healing elastomers. *Compos. Part B Eng.* **2023**, *248*, 110357. [CrossRef]

35. Garcia-Gonzalez, D.; Hossain, M. Microstructural modelling of hard-magnetic soft materials: Dipole–dipole interactions versus Zeeman effect. *Extrem. Mech. Lett.* **2021**, *48*, 101382. [CrossRef]

36. Sundar, U.; Lao, Z.C.; Cook-Chennault, K. Enhanced Dielectric Permittivity of Optimized Surface Modified of Barium Titanate Nanocomposites. *Polymers* **2020**, *12*, 26. [CrossRef]

37. Li, W.; Palardy, G. Electro-Mechanical response of Ultrasonically Welded Thermoplastic Composite interfaces under Static and cyclic Flexural loads using nanocomposites. *ACS Appl. Polym. Mater.* **2022**, *4*, 5209–5223. [CrossRef]

38. Ghabezi, P.; Sam-Daliri, O.; Flanagan, T.; Walls, M.; Harrison, N.M. Circular economy innovation: A deep investigation on 3D printing of industrial waste polypropylene and carbon fibre composites. Resources. *Conserv. Recycl.* **2024**, *206*, 107667. [CrossRef]

39. Li, L.; Zheng, S.X. Enhancement of dielectric constants of epoxy thermosets via a fine dispersion of barium titanate nanoparticles. *J. Appl. Polym. Sci.* **2016**, *133*, 10. [CrossRef]

40. Lijima, M.; Sato, N.; Lenggoro, I.W.; Kamiya, H. Surface modification of $BaTiO_3$ particles by silane coupling agents in different solvents and their effect on dielectric properties of $BaTiO_3$/epoxy composites. *Colloids Surf. A Physicochem. Eng. Asp.* **2009**, *352*, 88–93.

41. Badheka, P.; Magadala, V.; Devaraju, N.G.; Lee, B.I.; Kim, E.S. Effect of dehydroxylation of hydrothermal barium titanate on dielectric properties in polystyrene composite. *J. Appl. Polym. Sci.* **2006**, *99*, 2815–2821. [CrossRef]

42. Leigh, S.J.; Bradley, R.J.; Purssell, C.P.; Billson, D.R.; Hutchins, D.A. A Simple, Low-Cost Conductive Composite Material for 3D Printing of Electronic Sensors. *PLoS ONE* **2012**, *7*, 49365. [CrossRef]

43. Laureto, J.; Tomasi, J.; King, J.A.; Pearce, J.M. Thermal properties of 3-D printed polylactic acid-metal composites. *Prog. Addit. Manuf.* **2017**, *2*, 57–71. [CrossRef]

44. Daminabo, S.C.; Goel, S.; Grammatikos, S.A.; Nezhad, H.Y.; Thakur, V.K. Fused deposition modeling-based additive manufacturing (3D printing): Techniques for polymer material systems. *Mater. Today Chem.* **2020**, *16*, 100248. [CrossRef]

45. Tensile Test Methods for Plastics: ASTM D638. Available online: https://www.shimadzu.eu/industry/hpi/tensile-638 (accessed on 1 February 2023).

46. Mgbemena, C.O.; Li, D.; Lin, M.F.; Liddel, P.D.; Katnam, K.B.; Thakur, V.K.; Yazdani Nezhad, H. Accelerated microwave curing of fibre-reinforced thermoset polymer composites for structural applications: A review of scientific challenges. *Compos. Part A Appl. Sci. Manuf.* **2018**, *115*, 88–103. [CrossRef]
47. Mishra, R.K.; Li, D.; Chianella, I.; Goel, S.; Lotfian, S.; Yazdani Nezhad, H. Low electric field induction in BaTiO$_3$-epoxy nanocomposites. *Funct. Compos. Mater.* **2023**, *4*, 6. [CrossRef]